Appl. Phys. A 60, 247–254 (1995)

Applied Physics A Materials Science & Processing

Angle-resolved photoemission experiments on $Bi_2Sr_2CaCu_2O_{8+\delta}$(001)

Effects of the incommensurate lattice modulation

J. Osterwalder[1,*], P. Aebi[1], P. Schwaller[1], L.Schlapbach[1], M. Shimoda[2], T. Mochiku[2], K. Kadowaki[2]

[1]Institut de Physique, Université de Fribourg, CH-1700 Fribourg, Switzerland
(Fax: + 41-37/82-6519)
[2]National Research Institute for Metals, 1-2-2 Sengen, Tsukuba, Ibaraki 305, Japan

Received: 13 June 1994/Accepted: 11 September 1994

Abstract. Core-level X-ray photoelectron-diffraction patterns have been measured from cleaved $Bi_2Sr_2CaCu_2O_{8+\delta}$ (001) surfaces for all elements present in this compound. The incommensurate modulation along b ([010]) leads to a strong inequivalence of a- and b-directions for Bi, Sr and Cu photoelectrons, while Ca and O emission show less effect. Ultraviolet-photoemission experiments recording the emission intensity at the Fermi energy over a large solid angle are also presented, providing a direct mapping of the Fermi surface. A $c(2\times2)$ superstructure is observed on the Fermi surface suggesting antiferromagnetic correlations within the Cu–O planes. The effects of the lattice modulation are clearly observable at the Fermi energy, and they are enhanced for binding energies higher than a few tens of meV.

PACS: 71.25.Hc; 74.72.Hs; 79.60.Bm

Even though the incommensurate lattice modulation along the b-axis in the Bi-type High-Temperature Superconductors (HTS) has been recognized very early as an intrinsic structural peculiarity in the bulk [1–3] and at the surface [4–6] of these compounds, its interrelation with the superconductivity is not clear. Notably, this modulation is not a common feature to all HTS materials. In this context it is of great interest to know how this phenomenon affects the electronic structure, and in particular those electronic states that are close to the Fermi energy. Angle-resolved photoemission has evolved as the prime technique to obtain detailed information on these electronic bands [7–10], and only very recently Kelley et al. [11] have established that the incommensurate modulation makes itself noticeable in a pronounced anisotropy of oscillator strength of Cu–O band emission along ΓX and ΓY (a*- and b*-directions, respectively).

Very recently, our group has used a new mode of conducting an angle-resolved photoemission experiment in order to map the Fermi surface of $Bi_2Sr_2CaCu_2O_{8+\delta}$ (Bi-2212) directly [12]. The resulting Fermi surface was found to agree rather well with that calculated within the local-density approximation for the unmodulated structure [13, 14], with a few significant deviations: (i) an additional superstructure on the Fermi surface is observed suggesting antiferromagnetic correlations within the Cu–O planes; (ii) the Bi–O electron pockets near the $\bar{M}$ point are not seen; and (iii) there are distinct features that show a periodicity along the b-axis and not along a. It is this last observation that we want to further elaborate in this paper.

In order to relate these findings concerning the electronic structure directly to the incommensurate modulation, we first present X-ray Photoelectron-Diffraction (XPD) data taken from the same surfaces and providing a structural view of the near-surface region. Core-level photoelectrons from Bi, Sr, Ca, Cu, and O atoms are excited to kinetic energies of the order of 1 KeV and scatter off the atomic arrangement surrounding the photoemitters. The resulting angular distributions [15] are highly anisotropic and reflect the local lattice geometry. Again, we shall emphasize what is the signature of the lattice modulation along b.

1 Experimental

All photoemission experiments were carried out in a Vacuum Generators' ESCALAB Mark II spectrometer which is equipped with a two-axis sample goniometer permitting computer-controlled crystal rotation. An important asset of this system is that samples can be introduced by means of a load lock and in-situ mounted on the goniometer with 0.1° precision before cleaving. Therefore, no bakeout procedure is necessary while the crystals are inside the vacuum chamber, and the base pressure of 3×10^{-11} mbar is typically reached soon after the scotch-tape cleaving and removal of the tape through the load lock. For the XPD experiments, a twin anode was used producing either Mg-K_α (1253.6 eV) or Si-K_α (1740 eV)

* *New address*: Physik-Institut, Universität Zürich-Irchel, CH-8057 Zürich, Switzerland (Fax: + 41-1/257-5704)

radiation. Ultraviolet Photoelectron Spectroscopy (UPS) and Fermi-surface mapping were done with He I radiation (21.2 eV) from a discharge lamp. Special care was taken to maintain a stable operation of the lamp over extended measuring periods.

Complete angular distributions of photoelectrons excited by either X-ray or UV radiation were measured by sweeping the emission direction, i.e., the lens-analyzer entrance direction, over almost 2π solid angle relative to the crystal lattice by computer-controlled crystal rotation [16]. The angular resolution of the spectrometer was set to 1° full-acceptance cone. At each of typically 4000–6000 angular settings, the spectral range of interest is measured and, in the case of XPD, the signal intensity is evaluated by curve fitting. For obtaining a map of the Fermi surface, a very narrow energy window with a width of the order of the spectrometer resolution (20–30 meV) is centered at the Fermi energy (E_F) and the intensity within this window is recorded simultaneously with a background intensity, measured about 100 meV above E_F, which then is subtracted. This procedure makes sure that no contribution from He I satellite radiation contributes to the measured anisotropies. These full measurements typically took 24 to 48 h, and no sample degradation was observed in UPS spectra over many days up to a few weeks. The orientation of the main crystal axes, and in particular of the *a*- and *b*-directions, was measured independently by Low-Energy Electron Diffraction (LEED) and by XPD, the latter providing an accuracy in absolute positions of better than 1°.

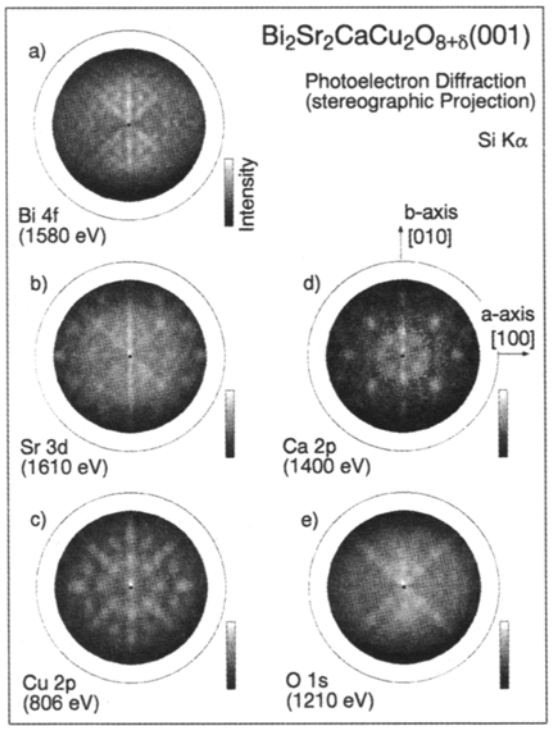

Fig. 1a-e. Stereographically projected XPD patterns of Bi 4*f*(**a**), Sr 3*d*(**b**), Cu 2*p*(**c**), Ca 2*p*(**d**), and O 1*s*(**e**) emission from Bi-2212, excited by Si-K_α radiation (1740 eV). The *black dots* in the center of each pattern indicate the surface normal, while the outer *circles* represent emission along the surface. Intensities are represented in a linear *grey scale*

2 Photoelectron-diffraction results

In Fig. 1, we present stereographically projected XPD data for Si-K_α-excited core levels of all five elements constituting this compound, with intensities given in a linear grey scale. Photoelectron kinetic energies range from 806 eV for Cu $2p_{3/2}$ emission to 1610 eV for Sr 3d emission. These rather high energies facilitate the interpretation of these data: It is well known that such angular distributions are dominated by the strong forward-scattering amplitudes of the individual electron–atom scattering processes [17–19]. As a result, each photoemitter produces a series of intensity maxima along emission directions passing through strongly scattering atoms within layers closer to the surface. To first approximation, the near-surface lattice is projected onto the solid-angle hemisphere, with only weak dependence of the patterns on the electron energy in the 1 keV region [16]. With this simple interpretation, the data of Fig. 1 become particularly informative: The crystal structure of Bi-2212 consists of a well-defined sequence of metal-oxide layers parallel to the surface (Fig. 2), and, therefore, each layer contains photoemitters of one particular metal. Taking into account that inelastic mean free paths of photoelectrons at these energies are typically 15–30 Å [20], the observed angular distributions are representative for the uppermost unit cell terminating the crystal, with roughly a negative-exponential weighting of photoemitters with depth.

It is generally accepted that the cleaved (001) surface of Bi-2212 is terminated by one Bi–O layer [4–6, 15]. Obviously, this top layer will not produce any forward-scattering- related anisotropy in Bi 4*f* emission, and the diffraction pattern will thus be dominated by Bi emitters 6 and 7 layers below the surface. In the simplest picture, these two types of photoemitters project one half unit cell of atoms onto the emission hemisphere producing a dense grid of forward-scattering maxima. The experimental pattern of Fig. 1a exhibits, indeed, a very rich pattern of maxima and lines of enhanced intensity. One should be cautioned, however, that such multilayer scattering processes may be considerably affected by multiple scattering, but its main effects have been recognized as an attenuation of forward-scattering anisotropies and a sharpening of the maxima [21, 22]. In any case, the simple projection-type interpretation provides an understanding of the effects of the incommensurate lattice modulation on the diffraction pattern. According to the structure refinement of the modulated structure given by Yamamoto et al. [3] on the basis of neutron and X-ray diffraction measurements, the modulated atomic displacements from the average Bi positions are particularly large along the b-direction. As is illustrated in Fig. 2, this means that, for Bi emitters, forward-scattering directions are considerably smeared out but remain within the *bc*-plane. Consequently, along the [010] azimuth, the Bi 4*f* diffraction pattern exhibits a strong line of enhanced intensity typical of emission along dense atomic planes [16]. No such line is observed along the [100] azimuth which defines the *ac*-planes. Here, the large displacements move Bi emitters out of the lattice plane

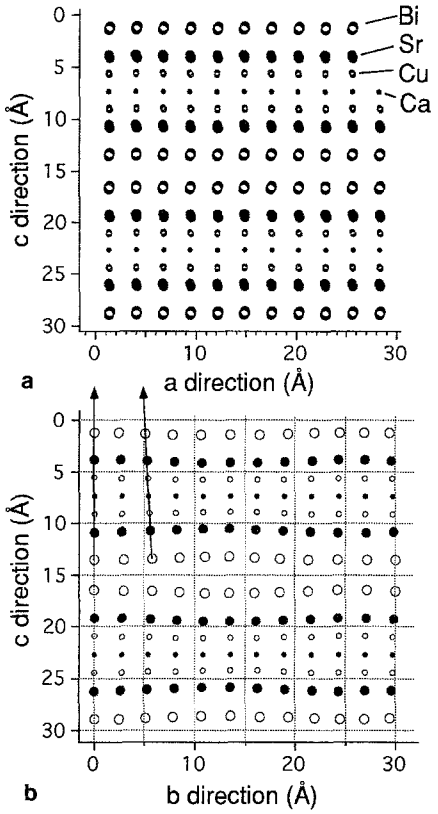

Fig. 2a, b. Projections of the modulated lattice positions onto the *ac*-plane (**a**) and the *bc*-plane (**b**) according to the structure model for Bi-2212 [3]. In (**a**), the slighly smeared-out *circles* indicate the small modulation amplitudes along the *a*- and *c*-directions. In (**b**), two *arrows* indicate the smearing out of forward-scattering directions in Bi 4*f* emission within the *bc*-plane

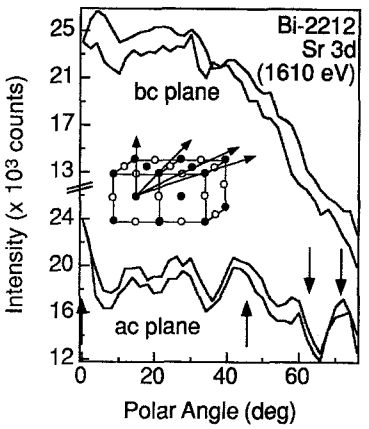

Fig. 3. Polar intensity scans of Sr 3*d* emission along the *ac*-plane (*bottom two curves*) and the *bc*-plane (*top two curves*) taken from the data of Fig. 1b. *Arrows* indicate polar angles of important forward-scattering directions within a NaCl-type metal-oxide lattice, which is given schematically in the *inset*

(Fig. 2), thinning out the forward-scattering enhancement along the plane.

Similar asymmetries between *a*- and *b*-directions are found in the diffraction patterns of Sr 3*d* and less so for Cu 2*p* and Ca 2*p*. In all cases, intense lines, modulated by forward-scattering peaks along low-index directions, appear along the [010] azimuth and no such lines along [100]. Moreover, fewer forward-scattering maxima are seen, reflecting the fact that dominant Sr or Cu photoemitters are closer to the surface than in the Bi case.

In Fig. 3, we have extracted four polar scans from the Sr 3*d* data of Fig. 1b, representing radial cuts along the [100], [$\bar{1}$00], [010] and [0$\bar{1}$0] azimuths. These cuts show pronounced diffraction maxima in the *ac*-plane and higher, but rather structureless intensities in the *bc*-plane. Two quite strong maxima appear at grazing angles along the [100] and [$\bar{1}$00] azimuths (Figs. 1b and 3). At such low take-off angles, the surface sensitivity of XPD is considerably enhanced, and these maxima should therefore be due to forward scattering of second-layer Sr photoelectrons off first-layer Bi atoms (Fig. 3, inset). The polar angle θ of these maxima should give a direct measure for the Bi–O/Sr–O layer spacing at the surface. We find $\theta = 73.0 \pm 0.5°$, and taking into account the photoelectron-wave refraction at the surface [17] due to an inner potential of the order of 15 eV, this value is slightly reduced to 72.2° inside the solid, giving a layer spacing of 2.60 ± 0.08 Å. This is to be compared with 2.7–2.8 Å for the bulk obtained by X-ray or neutron scattering [1, 3]. From considering the inset in Fig. 3, we should expect additional forward-scattering maxima along the same azimuths at polar angles of 0, 46 and 64°. These peaks are, indeed, observed in Fig. 3 as indicated by arrows, except for the Sr → O forward scattering at 64°. This may be explained either by the far weaker scattering potential of oxygen atoms or by considerable displacements of oxygen atoms away from ideal, NaCl-type positions, as discussed, e.g., by Yamamoto et al. [3].

Several other maxima found in the data of Fig. 1 can be directly related to important forward-scattering directions in a simple NaCl-type Me–O lattice, such as, e.g., the pronounced maxima at $\theta = 54°$ along the $< 110 >$ azimuths in both Sr 3*d* and Ca 2*p* emission. The Ca 2*p* data are particularly simple owing to the fact that it is essentially one single layer that dominates the emission pattern (Fig. 2).

It is much harder to extract any structural information from the O 1*s* emission pattern of Fig. 1e. Here, oxygen photoemitters are distributed over all layers and we measure an incoherent superpostion of many individual patterns. One significant observation is that there are no well-developed forward-scattering features parallel to the *ac*- and *bc*-planes, but rather pronounced intensity bands along the $< 110 >$ -type planes, with distinct maxima at $\theta = 54°$ and along the surface normal. These maxima represent the only remainders of a NaCl-type lattice, while we must infer substantial displacements of oxygen atoms out of the *ac*- and *bc*-planes defined by the metal positions.

Any further structural conclusions from this set of XPD data await a careful analysis by means of multiple-scattering calculations for various structure models. With currently available computer codes this represents a formidable task. The situation is still aggravated by our showing that the incommensurate lattice modulation strongly influences the diffraction pattern. For the scope of this paper, we content ourselves with concluding that these data permit us to unambiguously identify the surface

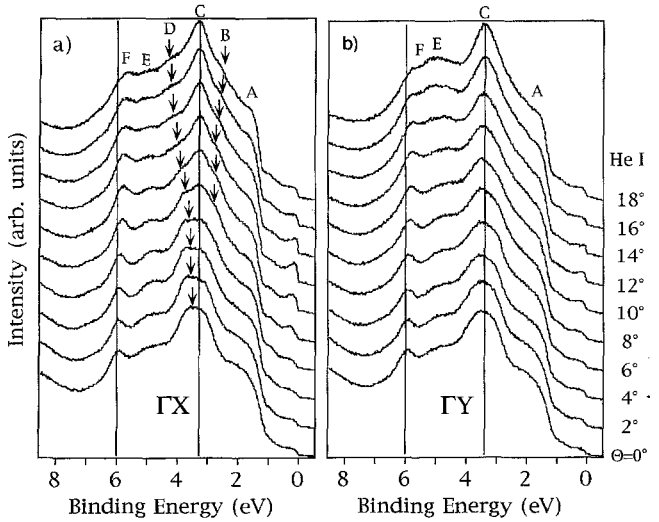

Fig. 4a, b. ARUPS spectra from Bi-2212, excited by He I radiation (21.2 eV). In (**a**), spectra measured in two-degree steps within the *ac*-plane (ΓX) are shown, beginning at the Γ-point (*bottom curve*). Letters *A* through *F* label strong spectral features, *arrows* indicate the dispersions of features *B* and *D*. In (**b**), the same measurements within the *bc*-plane (ΓY) are shown

termination [15] and to distinguish the *a*- and *b*- directions. Moreover, the observed patterns are qualitatively consistent with bulk-atomic displacements of the modulated structure determined by Yamamoto et al. [3]. We have, therefore, a sound structural basis for starting our discussion of the effects of the modulation on the electronic structure.

3 Angle-resolved ultraviolet photoemission

In Fig. 4, we give two sets of Angle-Resolved Ultraviolet Photoelectron Spectroscopy (ARUPS) data measured from a cleaved Bi-2212(001) surface along the ΓX- (Fig. 4a) and ΓY- (Fig. 4b) directions. The asymmetry between these two directions is apparent both in the region of the Fermi energy (E_F) and in the strong Valence-Band (VB) emission region ranging from 1.2 to 7 eV. Near E_F, we observe a dispersing transition from the Cu–O band along ΓX, crossing the Fermi level somewhere around 12°, while Cu–O band emission and dispersion is generally weaker along ΓY. This is fully consistent with the report of Kelley et al. [11]. In the VB emission region for binding energies higher than 1.2 eV we have, according to the band-structure calculations of Massidda et al. [13], a total of 48 bands of mostly Cu-*d* and O-*p* character. A discussion of the spectral features must here remain rather vague. Nevertheless, we observe significant spectral changes with emission angle along ΓX, with the strongest dispersion of the order of 0.5 eV shown by feature D (Fig. 4a). Again, dispersion effects are weaker along ΓY, and spectral changes are here mainly due to variations in relative intensities, such as, e.g., the increasing importance with polar angle of feature E relative to F and C (Fig. 4b). From these spectra, we can, therefore, conclude that there must be a strong signature of the modulation in the electronic structure of Bi-2212.

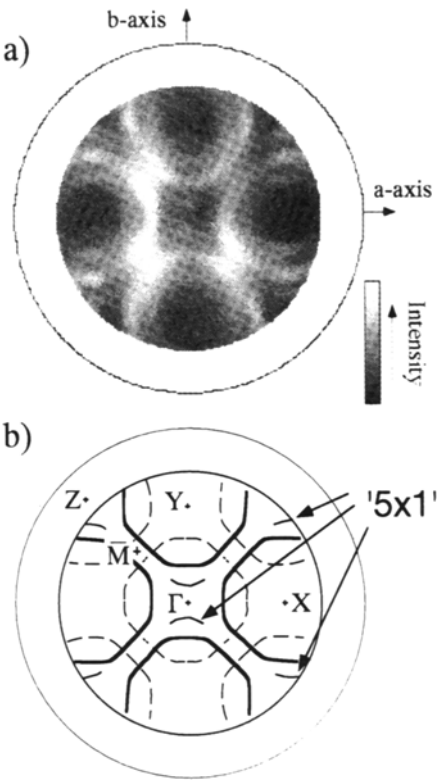

Fig. 5. **a** $k_\parallel$ mapping of the intensity of He I (21.2 eV) excited photoelectrons collected from Bi-2212(001) within an energy window of 10 meV width centered at the Fermi energy. A logarithmic intensity scale is used. The *outer circle* indicates emission along the surface. **b** Outline of **a**, emphasizing the fine lines observed in the measurement and distinguishing between the stronger (*thick lines*) and weaker (*thin lines*) sets of lines. Features that appear to be related to the lattice modulation are indicated by *arrows*

In Fig. 5a, we present the result of our Fermi-surface-mapping experiment on Bi-2212(001). In order to obtain this image, the absolute intensity of He I (21.2 eV) excited photoemission has been recorded within a very narrow energy window of 10 meV centered at E_F and then plotted in a logarithmic grey scale in parallel projection. A total of 5993 angular settings have been measured with an angular resolution of better than 1°. As discussed elsewhere [12, 23, 24], continuous lines are observed in such plots at locations where direct transitions move through the Fermi level, and the conservation of parallel momentum in photoemission relates these lines directly to the Fermi surface. For two-Dimensional (2D) systems the correspondence is one-to-one [23], while in three-Dimensional (3D) systems [24], one obtains sections through the 3D Fermi surface depending on the photon energy. The layered cuprates are generally considered as 2D systems, and we can, therefore, view the measurement of Fig. 5a as a direct map of the Fermi surface of Bi-2212.

We find a set of rather intense lines, which we represent in Fig. 5b by thick solid lines, and which agree rather well with the Fermi surface calculated by Massidda et al. within the local-density approximation [13]. The only exception is the region near the $\bar{M}$-point, where we observe two parallel sections of the Fermi surface with no indication of the Bi–O-related electron pockets and the

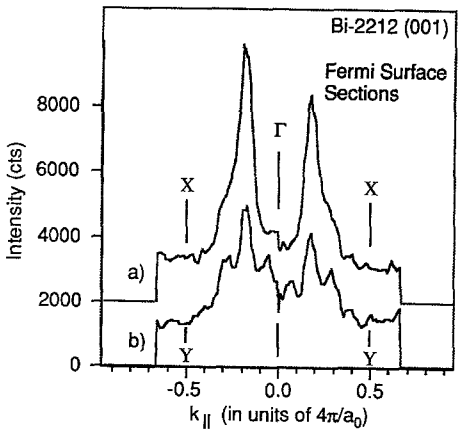

Fig. 6. Sections through the data of Fig. 5a, corresponding to cuts (*a*) $X\Gamma X$ and (*b*) $Y\Gamma Y$. The intensity scale is here linear

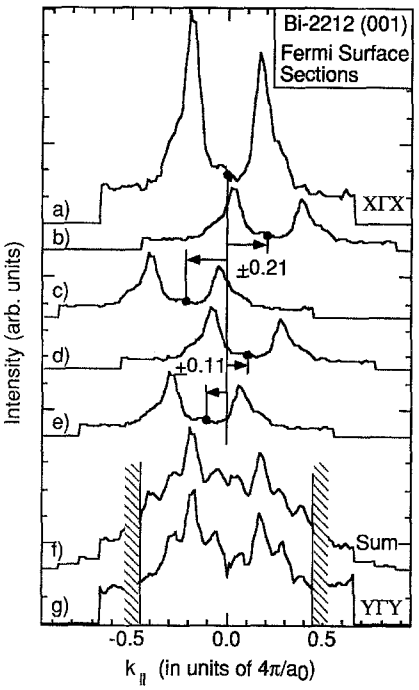

Fig. 7. Section $X\Gamma X$ through the data of Fig. 5a.; (*b–e*) give replicas of (*a*), as obtained by translations with vectors ± 0.212 and ± 0.106 in units of $4\pi/a_o$ and by multiplying with a factor of 0.3. In (*f*) the sum of all curves (*a–e*) is given (divided by 2) and compared to the experimental section $Y\Gamma Y$

associated repulsion of the Cu–O Fermi surface away from the $\bar{M}$-point.

Apart from this main Fermi surface, our measurement shows additional weaker lines, which we have accentuated by choosing a logarithmic grey scale in this figure. One continuous set is represented by dashed lines in Fig. 5b. They can be reproduced by a translation of the main Fermi surface by the vectors ΓX or ΓY, which are equivalent with the vector $(\pi/a, \pi/a)$, where a is the Cu–Cu distance within the Cu–O planes. In the language of surface science, this superstructure on the Fermi surface is of $c(2 \times 2)$ symmetry. Antiferromagnetic correlations within the Cu–O planes can account for this symmetry [12], and ARUPS should be sensitive to such magnetic effects through spin-dependent scattering amplitudes [25]. In fact, Kampf and Schrieffer [26] had predicted the occurrence of such "shadow bands" in photoemission due to antiferromagnetic spin fluctuations.

Again, we want to focus on the *a-b* asymmetry in these data. There are several weak features that appear to be related to translational symmetry along *b* only, and which we have pointed out in Fig. 5b by arrows marked "5 × 1". They consist of two banana-shaped structures just above and below the Γ-point and near the, in 2D equivalent, Z-points. The asymmetry is more clearly visible in Fig. 6, where we show two perpendicular line sections through the data of Fig. 5. The section along the a direction (Fig. 6a, $X\Gamma X$) exhibits two very strong maxima at $k_{\|} = \pm 0.18$ (in units of $4\pi/a_0$) due to the main Fermi surface and two shoulders at $k_{\|} = \pm 0.32$ associated with the shadow bands. Along the modulation direction (Fig. 6b, $Y\Gamma Y$), the main Fermi surface appears also at $k_{\|} = \pm 0.18$, though considerably weaker. Here, extra features are observed with high relative intensities. The maxima at ± 0.07 represent the banana-shaped structures, while the maxima at ± 0.3 may have a component due to the shadow band and possibly one related to the modulation. Different absolute intensities of symmetry-related features are a consequence of sample inhomogeneities, because different angular settings probe slightly different sample areas.

In order to understand the origin of the various extra features in the $Y\Gamma Y$ data, we simulate in Fig. 7 the folding of the Fermi surface, which is expected due to the periodicity of the modulation. As a reference for the unmodulated Fermi surface, we use the data along $X\Gamma X$ (Fig. 7a), which should be only weakly affected by the modulation, and which contains a weak contribution due to the $c(2 \times 2)$ short-range symmetry. According to Yamamoto et al. [3], incommensurate reciprocal lattice points are introduced along *b* spaced at distances of 0.2118 b^* starting from the Γ-point, which in units of $4\pi/a_0$ translates into 0.106 (the magnitude of b^* is roughly $2\pi/a_0$). We, therefore, expect additional Fermi surfaces shifted by ± 0.106 along ΓY (Fig. 7d, e) and by ± 0.212 (Fig. 7b, c) and so forth. In Fig. 7f, we show the result of the superposition of the $X\Gamma X$ Fermi surface (weight 1.0) with all ± 0.106 and ± 0.212 shifted Fermi surfaces of weight 0.3. Further incommensurate reciprocal lattice points, such as, e.g., at ± 0.318, were not considered. We obtain an excellent fit to the experimental $Y\Gamma Y$ Fermi surface (Fig. 7g) in peak positions and also relative intensities. Considering LEED patterns from these surfaces which image the 2D reciprocal lattice directly, one finds also that the intensities of the incommensurate superlattice spots are strongly modulated along b^* [27]. It is thus no surprise that we essentially observe the main Fermi surface and two adjacent super-Fermi surfaces along $\pm b^*$.

As a last point, we want to discuss the effects of the modulation on the measured band dispersion. For this purpose, we give in Fig. 8 a set of six intensity maps taken for narrow energy windows at different binding energies, ranging from 0 meV (Fermi surface) to 400 meV.

Other than in Fig. 5, the data have here no background subtracted and are given in a linear, not logarithmic, grey scale. In principle, these data should be directly related to constant energy surfaces [23]. However, we note that the discrete lines seen at E_F become gradually broad and diffuse at higher binding energies. A more complete interpretation of such data should, therefore, take into account the detailed shape of the spectral function, a task which can be done only qualitatively, and which is beyond the scope of this paper.

We can, nevertheless, observe distinct dispresion effects: The main Fermi surface centered at the Γ-point contracts towards Γ with increasing binding energy, which is consistent with band-structure calculations [13, 14]. Likewise, the shadow Fermi surfaces contract towards the X- and Y-points, which confirms the $c(2\times2)$ superstructure on the Fermi surface [12]. At 100 meV binding energy, the constant energy surface is still seen as a distinct line across the ΓX-direction, but along ΓY a deep intensity depression is formed with no internal structure. This pronounced a-b asymmetry grows with increasing binding energy. While the modulation represents in these images a relatively weak perturbation at E_F, its effects become rapidly more pronounced below E_F. One interpretation of this may be that the Fermi surface is defined exclusively by states localized within the Cu–O planes, where modulation amplitudes along the a- and b-directions are small (< 0.1 Å [3]), while other planes start contributing below E_F. This supposition of a highly 2D character of the Fermi surface is supported by the fact that we have no indication for the Bi–O electron pockets at the $\bar{M}$-point predicted by theory [13, 14].

An interesting question concerning quantitative dispersion has been raised by Claessen [28]. Considering positions of direct-transition peaks in experimental energy-distribution curves, the width of the occupied Cu–O band has been assigned to be of the order of 200–400 meV [7, 11, 29]. It has to be admitted that these peaks become extremely weak near the Γ-point, sitting on a high background. Our constant energy surfaces (Fig. 8) indicate a much larger bandwidth, since the observed lines across ΓX by no means approach the Γ-point at 400 meV binding energy (see also $X\Gamma X$ sections in Fig. 3 of [12]). Even though our spectra (Fig. 4) agree with those of other groups [7, 11, 29], our different measuring mode, which consists of recording the total photoemission intensity within a narrow energy window, appears to pick up a different dispersion function. This observation is rather interesting, although not too surprising. At the Fermi level, the dispersing quasiparticle peak sits on a low background of He II and He I satellite-excited and inelastically scattered photoelectrons which exhibit a weak and smooth angular dependence. The signal-to-background ratio decreases rapidly away from E_F and the quasiparticle peak, dispersing to higher binding energies, contributes only weakly to the measured intensity maps, while the dispersionless background dominates.

In order to elucidate further the influence of the spectral shape on the measured constant-energy maps, we show in Fig. 9 a series of energy spectra corresponding to various azimuthal emission angles for a fixed polar angle of $\theta = 39°$ off normal. In $k_\parallel$, the series starts near the $\Gamma\bar{M}$

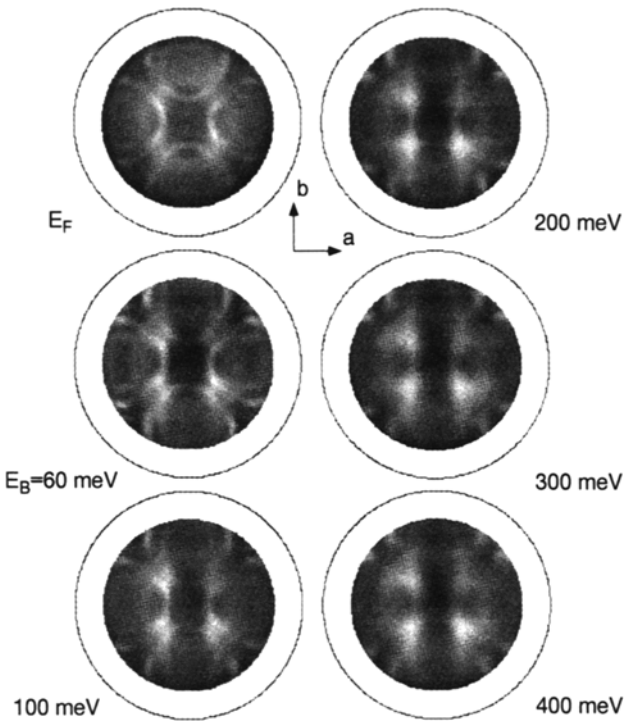

Fig. 8. $k_\parallel$ mappings of the photoelectron intensities from Bi-2212(001) measured within various binding-energy windows (E_B) of 10 meV width using He I radiation (21.2 eV). Intensities are given in a linear *grey scale*

azimuth (Fig. 5b) and sweeps in 1° steps along a circle towards the ΓX azimuth 45° away. The relatively high polar angle puts $k_\parallel$ far into the second Brillouin zone, cutting through the main Fermi surface as well as the shadow and "5×1" Fermi surfaces. All spectra are plotted without normalization of relative intensities [30], and vertical cuts along constant binding energies correspond thus directly to curved sections through the intensity maps of Fig. 8. We see the Fermi-level crossing due to the main Fermi surface in the center of Fig. 9a. The dispersive nature is brought out more clearly in the grey-scale representation of the spectra in Fig. 9b. The "5×1" Fermi surface appears as slightly enhanced emission at E_F near the bottom of Figs. 9a and b, while the $c(2\times2)$ shadow Fermi surface produces an even weaker increase in Fermi-level emission about half way between the main Fermi surface and the ΓX azimuth, more clearly visible in the grey-scale plot (Fig. 9b). The spectra of Fig. 9a illustrate that it is extremely difficult to extract anything but the main Fermi-surface transition from just the spectral shape, and that retaining absolute intensities is crucial. Moreover, we find that, as soon as the main transition appears at the Fermi level, the background intensity behind the peak increases dramatically. It is not clear whether this tail is due to inelastically scattered electrons or whether it is an intrinsic part of the spectral function. This behavior is fundamentally different from that found in the case of Cu single crystals [24, 31], where the intensities behind direct-transition peaks drop to a background level common to all angles.

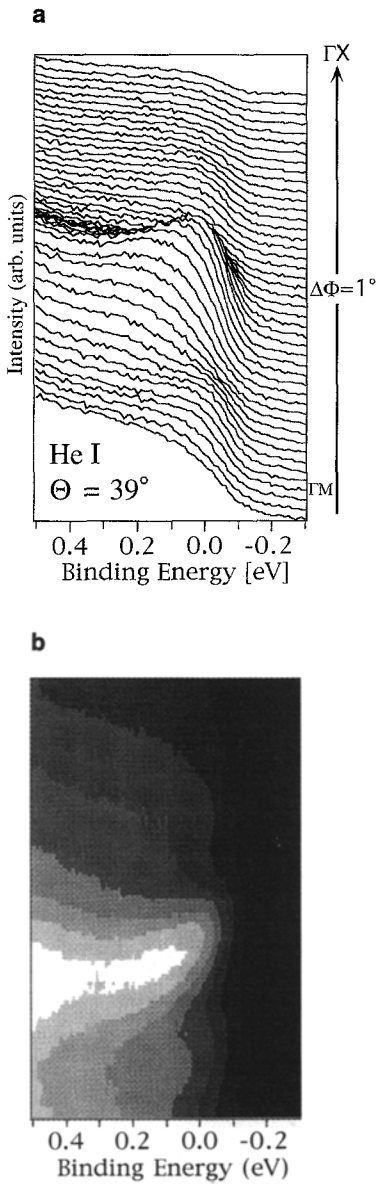

Fig. 9. a Energy spectra measured at a polar angle of 39° and for various azimuthal angles spaced 1° apart. These *angles* represent a circular section through the data of Figs. 5 and 8, beginning near the ΓM azimuth (which corresponds to the fourth curve from the bottom) and ending slightly before the ΓX azimuth. **b** The same spectra are represented in a linear *grey scale* which emphasizes the appearance of three features near the Fermi energy

4 Conclusions

Our XPD data strongly indicate that the near-surface structure of Bi-2212 is bulk-like, including the incommensurate modulation, and confirm the termination by a single Bi–O plane. Since the Cu–O layers are at least two layers below the surface layer, our ARUPS measurements are thus relevant for the current discussion of the electronic structure of the cuprates. In addition to a $c(2 \times 2)$ superstructure on the Fermi surface indicative of short-range antiferromagnetic correlations [12], we find a distinct signature of the quasi-5×1 lattice modulation. It appears as a nearly 5×1 superstructure along the b^*-direction, of which the first two superlattice points along either $\pm b^*$ contribute strongly, with weights of the order of 30% relative to that of the main Fermi surface. Unfortunately, the measured extra Fermi-surface contours are too broad and too diffuse in order to determine what happens at the new zone boundaries associated with the $c(2 \times 2)$ and quasi-5×1 periodicities.

Acknowledgements. We are greatful to R. Fasel, T. Kreutz and R. Claessen for stimulating discussions and to O. Raetzo, F. Bourqui, E. Mooser and H. Tschopp for excellent technical assistance. This work has been funded by the NFP30 of the Swiss National Foundation.

References

1. S.A. Sunshine, T. Siegrist, L.F. Schneemeyer, D.W. Murphy, R.J. Cava, B. Batlogg, R.B. van Dover, R.M. Fleming, S.H. Glarum, S. Nakahara, R. Farrow, J.J. Krajewski, S.M. Zahurak, J.V. Waszczak, J.H. Marshall, P. Marsh, L.W. Rupp, Jr., W.F. Peck: Phys. Rev. B **38**, 893 (1988)
2. Y. Le Page, W.R. McKinnon, J.-M. Tarascon, P. Barboux: Phys. Rev. B **40**, 6810 (1989)
3. A. Yamamoto, M. Onoda, E. Takayama-Muromachi, F. Izumi, T. Ishigaki, H. Asano: Phys. Rev. B **42**, 4228 (1990)
4. M.D. Kirk, J. Nogami, A.A. Baski, D.B. Mitzi, A. Kapitulnik, T.H. Geballe, C.F. Quate: Science **242,** 1673 (1988)
5. P.A.P. Lindberg, Z.-X. Shen, B.O. Wells, D.B. Mitzi, I. Lindau, W.E. Spicer, A. Kapitulnik: Appl. Phys. Lett. **53,** 2563 (1988)
6. C.K. Shih, R.M. Feenstra, J.R. Kirtley, G.V. Chandrashekhar: Phys. Rev. B **40,** 2682 (1989)
7. C.G. Olson, R. Liu, A.-B. Yang, D.W. Lynch, A.J. Arko, R.S. List, D.W. Veal, Y.C. Chang, P.-Z. Jiang, A.P. Paulikas: Science **245,** 731 (1989)
8. R. Manzke, T. Buslap, R. Claessen, J. Fink: Europhys. Lett. **9,** 477 (1989)
9. Y. Chang, M. Tang, R. Zononi, M. Onellion, R. Joynt, D.L. Huber, G. Margaritondo, P.A. Morris, W.A. Bonner, J.M. Tarascon, N.G. Stoffel: Phys. Rev. B **39,** 4740 (1989); Phys. Rev. Lett. **63,** 101 (1989)
10. D.S. Dessau, Z.-X. Shen, D.M. King, D.S. Marshall, L.W. Lombardo, P.H. Dickinson, A.G. Loeser, J. DiCarlo, C.-H. Park, A. Kapitulnik, W.E. Spicer: Phys. Rev. Lett. **71,** 2781 (1993)
11. R.J. Kelley, J. Ma, M. Onellion, M. Marsi, P. Alméras, H. Berger, G. Margaritondo: Phys. Rev. B **48,** 3534 (1993)
12. P. Aebi, J. Osterwalder, P. Schwaller, L. Schlapbach, M. Shimoda, T. Mochiku, K. Kadowaki: Phys. Rev. Lett. **72,** 2757 (1994)
13. S. Massidda, Jaejun Yu, A.J. Freeman: Physica C **158,** 251 (1988)
14. H. Krakauer, W.E. Pickett: Phys. Rev. Lett. **60,** 1665 (1988)
15. M. Shimoda, T. Greber, J. Osterwalder, L. Schlapbach: Physica C **196,** 236 (1992)
16. D. Naumovic, A. Stuck, T. Greber, J. Osterwalder, L. Schlapbach: Phys. Rev. B **47,** 7462 (1993)
17. C.S. Fadley: In *Synchroton Radiation Research: Advances in Surface Science*, ed. R.Z. Bachrach (Plenum, New York 1992) Chap. 11
18. W.F. Egelhoff, Jr.: Crit. Rev. Solid State Mater. Sci. **16,** 213 (1990)
19. H.C. Poon, S.Y. Tong: Phys. Rev. B **30,** 6211 (1984)
20. M.P. Seah, W.A. Dench: Surf. Interface Anal. **1,** 2 (1979)
21. S.Y. Tong, H.C. Poon, D.R. Snider: Phys. Rev. B **32,** 2096 (1985)
22. H.A. Aebischer, T. Greber, J. Osterwalder, A.P. Kaduwela, D.J. Friedman, G.S. Herman, C.S. Fadley: Surf. Sci. **239,** 261 (1990)
23. A. Santoni, L.J. Terminello, F.J. Himpsel, T. Takahashi: Appl. Phys. A **52,** 229 (1991)
24. P. Aebi, J. Osterwalder, R. Fasel, D. Naumovic, L. Schlapbach: Surf. Sci. **307/309,** 917 (1994)
25. J.A.D. Matthew: Phys. Rev. B **25,** 3326 (1982)

26. A.P. Kampf, J.R. Schrieffer: Phys. Rev. B **42,** 7967 (1990)
27. P.A.P. Lindberg, Z.-X. Shen, B.O. Wells, D.B. Mitzi, I. Lindau, W.E. Spicer, A. Kapitulnik: Appl. Phys. Lett. **53,** 2563 (1988)
28. R. Claessen: Privat communication
29. G. Mante, R. Claessen, T. Buslaps, S. Harm, R. Manzke, M. Skibowski, J. Fink: Z. Phys. B **80,** 181 (1990)
30. In fact, we have normalized the spectra using the 10 highest energy channels above the Fermi level. This procedure does not significantly change the relative intensities of the spectra in the region below E_F
31. P. Aebi, J. Osterwalder, D. Naumovic, R. Fasel, L. Schlapbach: Solid State Commun. **88,** 19 (1993)